

Search for Relativistic Magnetic Monopoles with IceCube

R. Abbasi,²⁸ Y. Abdou,²³ M. Ackermann,⁴² J. Adams,¹⁶ J. A. Aguilar,²² M. Ahlers,²⁸ D. Altmann,⁹ K. Andeen,²⁸ J. Auffenberg,²⁸ X. Bai,^{32,*} M. Baker,²⁸ S. W. Barwick,²⁴ V. Baum,²⁹ R. Bay,⁷ K. Beattie,⁸ J. J. Beatty,^{18,19} S. Bechet,¹³ J. Becker Tjus,¹⁰ K.-H. Becker,⁴¹ M. Bell,³⁹ M. L. Benabderrahmane,⁴² S. BenZvi,²⁸ J. Berdermann,⁴² P. Berghaus,⁴² D. Berley,¹⁷ E. Bernardini,⁴² D. Bertrand,¹³ D. Z. Besson,²⁶ D. Bindig,⁴¹ M. Bissok,¹ E. Blaufuss,¹⁷ J. Blumenthal,¹ D. J. Boersma,¹ C. Bohm,³⁵ D. Bose,¹⁴ S. Böser,¹¹ O. Botner,⁴⁰ L. Brayeur,¹⁴ A. M. Brown,¹⁶ R. Bruijn,²⁵ J. Brunner,⁴² S. Buitink,¹⁴ M. Carson,²³ J. Casey,⁵ M. Casier,¹⁴ D. Chirkin,²⁸ B. Christy,^{17,†} F. Clevermann,²⁰ S. Cohen,²⁵ D. F. Cowen,^{39,38} A. H. Cruz Silva,⁴² M. Danninger,³⁵ J. Daughhetee,⁵ J. C. Davis,¹⁸ C. De Clercq,¹⁴ F. Descamps,²⁸ P. Desiati,²⁸ G. de Vries-Uiterweerd,²³ T. DeYoung,³⁹ J. C. Díaz-Vélez,²⁸ J. Dreyer,¹⁰ J. P. Dumm,²⁸ M. Dunkman,³⁹ R. Eagan,³⁹ J. Eisch,²⁸ R. W. Ellsworth,¹⁷ O. Engdegård,⁴⁰ S. Euler,¹ P. A. Evenson,³² O. Fadiran,²⁸ A. R. Fazely,⁶ A. Fedynitch,¹⁰ J. Feintzeig,²⁸ T. Feusels,²³ K. Filimonov,⁷ C. Finley,³⁵ T. Fischer-Wasels,⁴¹ S. Flis,³⁵ A. Franckowiak,¹¹ R. Franke,⁴² K. Frantzen,²⁰ T. Fuchs,²⁰ T. K. Gaisser,³² J. Gallagher,²⁷ L. Gerhardt,^{8,7} L. Gladstone,²⁸ T. Glüsenskamp,⁴² A. Goldschmidt,⁸ J. A. Goodman,¹⁷ D. Góra,⁴² D. Grant,²¹ A. Groß,³¹ S. Grullon,²⁸ M. Gurtner,⁴¹ C. Ha,^{8,7} A. Haj Ismail,²³ A. Hallgren,⁴⁰ F. Halzen,²⁸ K. Hanson,¹³ D. Heereman,¹³ P. Heimann,¹ D. Heinen,¹ K. Helbing,⁴¹ R. Hellauer,¹⁷ S. Hickford,¹⁶ G. C. Hill,² K. D. Hoffman,¹⁷ R. Hoffmann,⁴¹ A. Homeier,¹¹ K. Hoshina,²⁸ W. Huelsnitz,^{17,‡} P. O. Hulth,³⁵ K. Hultqvist,³⁵ S. Hussain,³² A. Ishihara,¹⁵ E. Jacobi,⁴² J. Jacobsen,²⁸ G. S. Japaridze,⁴ O. Jlelati,²³ A. Kappes,⁹ T. Karg,⁴² A. Karle,²⁸ J. Kiryluk,³⁶ F. Kislak,⁴² J. Kläs,⁴¹ S. R. Klein,^{8,7} J.-H. Köhne,²⁰ G. Kohnen,³⁰ H. Kolanoski,⁹ L. Köpke,²⁹ C. Kopper,²⁸ S. Kopper,⁴¹ D. J. Koskinen,³⁹ M. Kowalski,¹¹ M. Krasberg,²⁸ G. Kroll,²⁹ J. Kunnen,¹⁴ N. Kurahashi,²⁸ T. Kuwabara,³² M. Labare,¹⁴ K. Laihem,¹ H. Landsman,²⁸ M. J. Larson,³⁷ R. Lauer,⁴² M. Lesiak-Bzdak,³⁶ J. Lünemann,²⁹ J. Madsen,³⁴ R. Maruyama,²⁸ K. Mase,¹⁵ H. S. Matis,⁸ F. McNally,²⁸ K. Meagher,¹⁷ M. Merck,²⁸ P. Mészáros,^{38,39} T. Meures,¹³ S. Miarecki,^{8,7} E. Middell,⁴² N. Milke,²⁰ J. Miller,¹⁴ L. Mohrmann,⁴² T. Montaruli,^{22,§} R. Morse,²⁸ S. M. Movit,³⁸ R. Nahnauer,⁴² U. Naumann,⁴¹ S. C. Nowicki,²¹ D. R. Nygren,⁸ A. Obertacke,⁴¹ S. Odrowski,³¹ A. Olivás,¹⁷ M. Olivo,¹⁰ A. O'Murchadha,¹³ S. Panknin,¹¹ L. Paul,¹ J. A. Pepper,³⁷ C. Pérez de los Heros,⁴⁰ D. Pieloth,²⁰ N. Pirk,⁴² J. Posselt,⁴¹ P. B. Price,⁷ G. T. Przybylski,⁸ L. Rädcl,¹ K. Rawlins,³ P. Redl,¹⁷ E. Resconi,³¹ W. Rhode,²⁰ M. Ribordy,²⁵ M. Richman,¹⁷ B. Riedel,²⁸ J. P. Rodrigues,²⁸ F. Rothmaier,²⁹ C. Rott,¹⁸ T. Ruhe,²⁰ B. Ruzybayev,³² D. Ryckbosch,²³ S. M. Saba,¹⁰ T. Salameh,³⁹ H.-G. Sander,²⁹ M. Santander,²⁸ S. Sarkar,³³ K. Schatto,²⁹ M. Scheel,¹ F. Scheriau,²⁰ T. Schmidt,¹⁷ M. Schmitz,²⁰ S. Schoenen,¹ S. Schöneberg,¹⁰ L. Schönherr,¹ A. Schönwald,⁴² A. Schukraft,¹ L. Schulte,¹¹ O. Schulz,³¹ D. Seckel,³² S. H. Seo,³⁵ Y. Sestayo,³¹ S. Seunarine,¹² M. W. E. Smith,³⁹ M. Soiron,¹ D. Soldin,⁴¹ G. M. Spiczak,³⁴ C. Spiering,⁴² M. Stamatikos,^{18,¶} T. Stanev,³² A. Stasik,¹¹ T. Stezelberger,⁸ R. G. Stokstad,⁸ A. Stöbl,⁴² E. A. Strahler,¹⁴ R. Ström,⁴⁰ G. W. Sullivan,¹⁷ H. Taavola,⁴⁰ I. Taboada,⁵ A. Tamburro,³² S. Ter-Antonyan,⁶ S. Tilav,³² P. A. Toale,³⁷ S. Toscano,²⁸ M. Usner,¹¹ D. van der Drift,^{8,7} N. van Eijndhoven,¹⁴ A. Van Overloop,²³ J. van Santen,²⁸ M. Vehring,¹ M. Voge,¹¹ C. Walck,³⁵ T. Waldenmaier,⁹ M. Wallraff,¹ M. Walter,⁴² R. Wasserman,³⁹ Ch. Weaver,²⁸ C. Wendt,²⁸ S. Westerhoff,²⁸ N. Whitehorn,²⁸ K. Wiebe,²⁹ C. H. Wiebusch,¹ D. R. Williams,³⁷ H. Wissing,¹⁷ M. Wolf,³⁵ T. R. Wood,²¹ K. Woschnagg,⁷ C. Xu,³² D. L. Xu,³⁷ X. W. Xu,⁶ J. P. Yanez,⁴² G. Yodh,²⁴ S. Yoshida,¹⁵ P. Zarzhitsky,³⁷ J. Ziemann,²⁰ A. Zilles,¹ and M. Zoll³⁵

(IceCube Collaboration)

¹III. Physikalisches Institut, RWTH Aachen University, D-52056 Aachen, Germany

²School of Chemistry & Physics, University of Adelaide, Adelaide SA, 5005 Australia

³Dept. of Physics and Astronomy, University of Alaska Anchorage, 3211 Providence Dr., Anchorage, AK 99508, USA

⁴CTSPS, Clark-Atlanta University, Atlanta, GA 30314, USA

⁵School of Physics and Center for Relativistic Astrophysics, Georgia Institute of Technology, Atlanta, GA 30332, USA

⁶Dept. of Physics, Southern University, Baton Rouge, LA 70813, USA

⁷Dept. of Physics, University of California, Berkeley, CA 94720, USA

⁸Lawrence Berkeley National Laboratory, Berkeley, CA 94720, USA

⁹Institut für Physik, Humboldt-Universität zu Berlin, D-12489 Berlin, Germany

¹⁰Fakultät für Physik & Astronomie, Ruhr-Universität Bochum, D-44780 Bochum, Germany

¹¹Physikalisches Institut, Universität Bonn, Nussallee 12, D-53115 Bonn, Germany

¹²Dept. of Physics, University of the West Indies,

Cave Hill Campus, Bridgetown BB11000, Barbados

¹³Université Libre de Bruxelles, Science Faculty CP230, B-1050 Brussels, Belgium

¹⁴Vrije Universiteit Brussel, Dienst ELEM, B-1050 Brussels, Belgium

- ¹⁵*Dept. of Physics, Chiba University, Chiba 263-8522, Japan*
- ¹⁶*Dept. of Physics and Astronomy, University of Canterbury, Private Bag 4800, Christchurch, New Zealand*
- ¹⁷*Dept. of Physics, University of Maryland, College Park, MD 20742, USA*
- ¹⁸*Dept. of Physics and Center for Cosmology and Astro-Particle Physics, Ohio State University, Columbus, OH 43210, USA*
- ¹⁹*Dept. of Astronomy, Ohio State University, Columbus, OH 43210, USA*
- ²⁰*Dept. of Physics, TU Dortmund University, D-44221 Dortmund, Germany*
- ²¹*Dept. of Physics, University of Alberta, Edmonton, Alberta, Canada T6G 2G7*
- ²²*Département de physique nucléaire et corpusculaire, Université de Genève, CH-1211 Genève, Switzerland*
- ²³*Dept. of Physics and Astronomy, University of Gent, B-9000 Gent, Belgium*
- ²⁴*Dept. of Physics and Astronomy, University of California, Irvine, CA 92697, USA*
- ²⁵*Laboratory for High Energy Physics, École Polytechnique Fédérale, CH-1015 Lausanne, Switzerland*
- ²⁶*Dept. of Physics and Astronomy, University of Kansas, Lawrence, KS 66045, USA*
- ²⁷*Dept. of Astronomy, University of Wisconsin, Madison, WI 53706, USA*
- ²⁸*Dept. of Physics and Wisconsin IceCube Particle Astrophysics Center, University of Wisconsin, Madison, WI 53706, USA*
- ²⁹*Institute of Physics, University of Mainz, Staudinger Weg 7, D-55099 Mainz, Germany*
- ³⁰*Université de Mons, 7000 Mons, Belgium*
- ³¹*T.U. Munich, D-85748 Garching, Germany*
- ³²*Bartol Research Institute and Department of Physics and Astronomy, University of Delaware, Newark, DE 19716, USA*
- ³³*Dept. of Physics, University of Oxford, 1 Keble Road, Oxford OX1 3NP, UK*
- ³⁴*Dept. of Physics, University of Wisconsin, River Falls, WI 54022, USA*
- ³⁵*Oskar Klein Centre and Dept. of Physics, Stockholm University, SE-10691 Stockholm, Sweden*
- ³⁶*Department of Physics and Astronomy, Stony Brook University, Stony Brook, NY 11794-3800, USA*
- ³⁷*Dept. of Physics and Astronomy, University of Alabama, Tuscaloosa, AL 35487, USA*
- ³⁸*Dept. of Astronomy and Astrophysics, Pennsylvania State University, University Park, PA 16802, USA*
- ³⁹*Dept. of Physics, Pennsylvania State University, University Park, PA 16802, USA*
- ⁴⁰*Dept. of Physics and Astronomy, Uppsala University, Box 516, S-75120 Uppsala, Sweden*
- ⁴¹*Dept. of Physics, University of Wuppertal, D-42119 Wuppertal, Germany*
- ⁴²*DESY, D-15735 Zeuthen, Germany*
- (Dated: November 20, 2012)

We present the first results in the search for relativistic magnetic monopoles with the IceCube detector, a subsurface neutrino telescope located in the South Polar ice cap containing a volume of 1 km^3 . This analysis searches data taken on the partially completed detector during 2007 when roughly 0.2 km^3 of ice was instrumented. The lack of candidate events leads to an upper limit on the flux of relativistic magnetic monopoles of $\Phi_{90\% \text{C.L.}} \sim 3 \times 10^{-18} \text{ cm}^{-2} \text{ sr}^{-1} \text{ s}^{-1}$ for $\beta \geq 0.8$. This is a factor of 4 improvement over the previous best experimental flux limits up to a Lorentz boost γ below 10^7 . This result is then interpreted for a wide range of mass and kinetic energy values.

PACS numbers: 14.80.Hv

I. INTRODUCTION

Magnetic monopoles are an important element in a complete picture of our universe. Their existence would explain the quantization of electric (and magnetic) charge via the Dirac quantization equation $g = Ne/2\alpha$ [1]. They appear as topological defects from symmetry breaking in Grand Unified Theories (GUTs) [2] with masses $\sim 10^4 - 10^{17} \text{ GeV}$ [3], depending on the breaking scheme.

Additionally, they would bring a complete symmetry to Maxwell's equations.

Magnetic monopoles produced in the early universe via GUT symmetry breaking would be topologically stable and accelerated along magnetic field lines. The universe is full of long range magnetic fields that would act upon the monopoles over their lifetime, likely imparting energies $\sim 10^{15} \text{ GeV}$ [3]. Therefore, magnetic monopoles below this energy scale should reach and travel through the Earth at relativistic speeds. A relativistic magnetic monopole moving through a transparent medium would produce copious amounts of Cherenkov light, ~ 8300 times a single muon in ice [4]. Thus, large Cherenkov detectors like IceCube are an ideal experiment to search for these particles.

The current best limits on the flux of magnetic monopoles at the 90% confidence level (C.L.) for relativistic speeds between $\beta = 0.8$ and Lorentz boost

*Physics Department, South Dakota School of Mines and Technology, Rapid City, SD 57701, USA

†Corresponding Author: email brian.christy@fandm.edu

‡Los Alamos National Laboratory, Los Alamos, NM 87545, USA

§also Sezione INFN, Dipartimento di Fisica, I-70126, Bari, Italy

¶NASA Goddard Space Flight Center, Greenbelt, MD 20771, USA

$\gamma = 10^7$ are set by the ANTARES detector [5] at the $\sim 10^{-17} \text{cm}^{-2} \text{sr}^{-1} \text{s}^{-1}$ scale. This recent result is the first in this velocity range to surpass the results from the AMANDA detector [6], IceCube's proof of concept, which set flux limits $\sim 3 \times 10^{-17} \text{cm}^{-2} \text{sr}^{-1} \text{s}^{-1}$. ANTARES also searched for magnetic monopoles below the Cherenkov threshold but still energetic enough to knock off electrons that produce Cherenkov light. This extension sets flux limits at the $\sim 5 \times 10^{-17} \text{cm}^{-2} \text{sr}^{-1} \text{s}^{-1}$ scale down to a speed of $\beta = 0.625$. For lower speeds, MACRO provides comprehensive flux limits $\sim 10^{-16} \text{cm}^{-2} \text{sr}^{-1} \text{s}^{-1}$ [7] for speeds down to $\beta \sim 10^{-4}$ while flux limits at ultra-relativistic speeds are set by radio detectors RICE [8] and ANITA [9] at the $\sim 10^{-19} \text{cm}^{-2} \text{sr}^{-1} \text{s}^{-1}$ scale.

These are important as they are flux limits below the 'Parker Bound' [10] ($\sim 10^{-15} \text{cm}^{-2} \text{sr}^{-1} \text{s}^{-1}$), an astrophysical flux limit derived by considering the survival of the galactic magnetic field in the presence of magnetic monopoles. More sophisticated calculations that consider velocity [11] relax the bound on relativistic magnetic monopoles above a mass of 10^{11}GeV due to the shortened time spent in the galactic field. However, an 'Extended Parker Bound' found by considering the survival of a modeled seed field still produces flux limits well below experiments, with $\Phi \sim 10^{-16} (\text{Mass}_{\text{MP}}) / (10^{17} \text{GeV}) \text{cm}^{-2} \text{sr}^{-1} \text{s}^{-1}$ [12].

This paper describes the search for relativistic magnetic monopoles in data taken with the IceCube detector between May 2007 and April 2008. The analysis is optimized for magnetic monopoles with modest Lorentz boosts ($\gamma \leq 10$) and charge $g = 1$. The derived flux limits are conservative upper bounds for magnetic monopoles with larger γ or charge, as these cases produce more light in the ice. The paper is organized as follows. Section II describes the IceCube detector. Section III describes the simulation of background and signal. Section IV defines the variables and outlines the steps used to discriminate signal events from background. Section V summarizes the uncertainties. Section VI presents the results for an isotropic flux of magnetic monopoles at the detector. Section VII extends this result to an isotropic flux at the Earth's surface by considering the energy loss of magnetic monopoles through the Earth. This results in a final limit plot that is presented over a large range of magnetic mass and kinetic energy values. This allows the result to remain agnostic towards the particular origin and energy gaining mechanism a magnetic monopole may possess. Concluding remarks are presented in Section VIII.

II. ICECUBE DETECTOR

IceCube is a telescope at the South Pole which detects neutrinos by measuring the Cherenkov light from secondary charged particles produced in neutrino-nucleon interactions [13]. A total of 5160 Digital Optical Modules (DOMs) are arranged in 86 vertical strings frozen in

the ice between 1500 and 2500 m below the surface over a total volume of 1km^3 . Construction was completed in December 2010. The data for this analysis were taken during the construction phase, when only 22 of the 86 strings had been deployed. The 22 strings contain a volume of $\sim 0.2 \text{km}^3$.

The DOM is the centerpiece of the IceCube detector and houses a 10-inch photomultiplier tube (PMT) to detect light, onboard electronics for pulse digitization, and LED light sources for calibration. Light signals which pass a threshold of 0.25 photo-electron (PE) PMT pulse heights are digitized and the DOM is said to 'launch'. Two types of waveform digitizers are utilized. The Analog Transient Waveform Digitizer (ATWD) bins the waveform with a 3.3 ns sampling period over a read-out window of 420 ns. It supports three channels with different gains in order to extend its effective dynamic range. The PMT Analog to Digital Converter (ADC) collects data at a slower sampling rate of 25 ns and records for $6.4 \mu\text{s}$.

A time is calculated for the launch by re-syncing the threshold crossing to the next leading edge of the internal DOM clock, which oscillates at 40 MHz. More precise timing is achieved by later reconstructing the leading edge of the digitized waveform, though in this analysis the coarse time is sufficient. For more information on the DOM and its components, see [14, 15].

Each waveform digitizer outputs the signal in terms of counts/bin values that directly map to the voltage recorded. For the PMT ADC, which is the only channel used in this analysis, a single photo-electron corresponds to ~ 13 counts [14]. The PMT ADC saturates at 1024 counts, which occurs when $\sim 50 - 100$ PE's arrive in a single 25 ns bin. More generally, DOM's that receive ~ 600 PE's over the full readout window typically saturate. Figure 1 shows example PMT ADC waveforms for both background and signal events at various distances to the DOM. The flattened top for the signal indicates the point where the digitizer saturates.

Once a launch is recorded, the DOM checks the four nearest neighbors on the string to see if another hit occurred within a $1 \mu\text{s}$ time window. By requiring companion launches to occur, the effect of dark noise hits is reduced. If this local coincidence condition is met, the digitized waveforms and time are sent to the surface. A trigger algorithm is applied to determine if a physics event has been detected. For the 22 string detector, this algorithm checked if 8 hits were recorded within a sliding $5 \mu\text{s}$ time window. For data in this analysis, the average trigger rate is $\sim 550 \text{Hz}$ and is vastly dominated by muons generated in cosmic ray air showers in the atmosphere above the South Pole.

Against this background a magnetic monopole event would stand out due to the much higher light deposition. For this analysis a further filter is applied to the data online at the South Pole, requiring at least 80 DOM launches in an event [16]. This retains all bright events, regardless of direction. The passing rate for this filter is

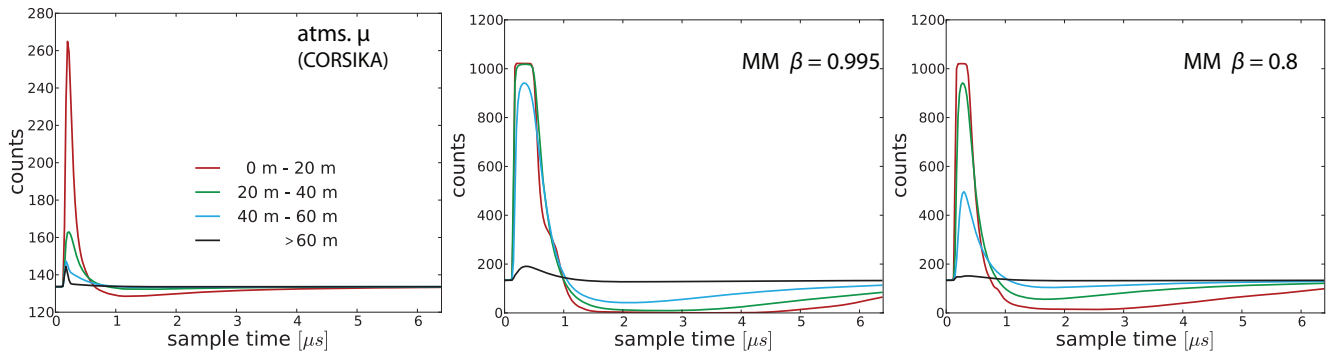


FIG. 1: Averaged PMT ADC waveforms for 1000 simulated events of atmospheric muon background (left) as well as the $\beta = 0.995$ (middle) and $\beta = 0.8$ (right) magnetic monopoles. Distances are how far away the particle is from the DOM receiving the light.

~ 1.5 Hz. It consists of muon bundles containing hundreds of muons generated by high energy cosmic ray primaries. All data that pass this filter are sent north via satellite to a data warehouse for use by the entire collaboration.

III. SIMULATION OF DATASETS

Simulation of the background and signal are done within the ICETRAY framework, a C++ based code written for use by the IceCube Collaboration. It includes tools to simulate the detector response to light produced by particles as well as the triggering and filtering algorithms. This allows simulated events to be compared directly to the experimental data.

A. Background Datasets

Background simulation is composed of muon bundles and neutrinos produced in the atmosphere by high energy cosmic rays. The generation uses importance sampling in energy so that at the final analysis level the statistical uncertainty in background prediction is of the order of systematic uncertainty or less.

Atmospheric muon bundles are simulated with CORSIKA [17] using two primary types: proton to represent light elements and iron to represent heavier ions. Primary energies are simulated between 10^4 and 10^{11} GeV. Events are generated with an E^{-2} spectrum to oversample the high energy region. The events are weighted to fits of extensive air showers introduced by the KASCADE Collaboration [18]. The muon bundles are then propagated through the ice using MMC (Muon Monte Carlo) [19].

ANIS (All Neutrino Interaction Simulation) [20] is used to simulate both muon and electron neutrino events. The neutrinos are generated with an E^{-1} spectrum and given weights corresponding to a conventional atmospheric neutrino flux from Honda [21] and a prompt flux

from charmed meson production based on the Enberg, Reno, and Sarcevic model [22].

B. Signal Datasets

Code developed specifically for this analysis is used to generate and propagate the signal magnetic monopoles. Three datasets are created for discrete speeds of $\beta = 0.8, 0.9$ and 0.995 ($\gamma = 10$). Monopole tracks are generated by randomly distributing vertices on a circular “generation plane” with radius 650 m at a distance of 1000 m from the detector center. From the vertices, monopoles are propagated towards and through the detector with directions perpendicular to the plane. During generation, the orientations of the generation plane relative to the detector are randomized, thereby creating an isotropic monopole flux through the detector.

Above $\beta \sim 0.1$ and below $\gamma \sim 10^4$, the electromagnetic energy loss of magnetic monopoles through matter is well described by a combination of ionization and atomic excitations, collectively referred to as ‘collisional’ energy loss [23]. As the choice of simulated events only reach $\gamma = 10$, this is the only energy loss considered in propagation. Above $\gamma \sim 10^4$, energy losses from pair production and photo-nuclear interactions surpass the collisional losses. These energy losses are considered in Section VII A for magnetic monopoles traveling through the Earth with large boost factors. Bremsstrahlung, which is proportional to $1/M^2$, is heavily suppressed.

For each dataset, 100,000 events are generated at a mass of $M = 10^{11}$ GeV. The effect of choosing one mass is mitigated since the Cherenkov light output only depends on speed which remains essentially constant over the 1.2 km path through the detector.

IV. EVENT SELECTION

The main strategy employed to select relativistic magnetic monopoles is to look for extremely bright events.

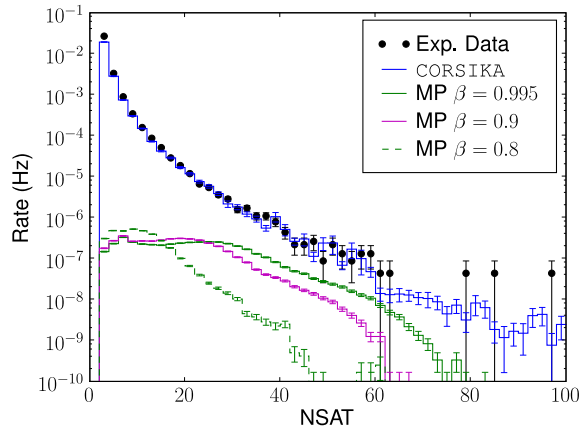


FIG. 2: The number of saturated hits per event for the simulated signal and atmospheric muon background (CORSIKA). In addition, the full experimental data set is included.

This is measured by counting the number of DOM launches which capture a high charge. High charge DOM launches are defined as ones that saturate the PMT ADC channel. Figure 2 shows the number of these “saturated hits” (NSAT). To visualize the signal event rates, a flux of $5 \times 10^{-17} \text{cm}^{-2} \text{sr}^{-1} \text{s}^{-1}$ is used.

A secondary strategy is to exploit the arrival directions of the incoming particle tracks. The dominant background of atmospheric muon bundles can only reach the detector from above the horizon. This background can be suppressed by focusing on events with arrival directions below the horizon.

Event selection consists of three phases. First, a simple filter is applied to reduce the data to a manageable size. Then, particle tracks are reconstructed and poorly reconstructed events are rejected using quality cuts. At the final stage, an optimized cut which maximizes the Model Rejection Factor (MRF) [24] is found. To reduce experimenter bias, the maximized MRF is found using simulated background alone. The resulting cut is then applied to the experimental data.

Table I displays the final event rates (in events/year) for each of the datasets considered at all levels of the analysis.

A. Track Reconstruction

Since directional information is used mainly to distinguish between up and down-going particles, pointing accuracy is only of secondary importance. Contrary to most IceCube analyses, which use computationally intensive likelihood methods to reconstruct the particle tracks with sub-degree accuracy, a very fast analytic fit proved sufficient for this analysis.

The fundamental piece of datum used by the reconstruction is a “hit”, which is defined as the location \vec{X}

and a time t of a DOM launch. The track direction and particle speed are reconstructed by a least-squares fit of the observed hit pattern $\{\vec{X}_i, t_i\}$ to a plane wave of light, whose analytic solution is given by [25]

$$\vec{X} = \vec{X}_{\text{avg}} + \vec{V}t \quad (1)$$

$$\vec{V} = \frac{\sum (\vec{X}_i - \vec{X}_{\text{avg}})(t_i - t_{\text{avg}})}{\sum (t_i - t_{\text{avg}})^2} \quad (2)$$

where \vec{X}_{avg} and t_{avg} are the average position and time of all the hits. The hit times t_i correspond to the time at which the DOM records a launch. Studies of the reconstruction accuracy demonstrated this to be a better definition for t_i than the peak time of the PMT pulse, likely because the launch time corresponds to the arrival time of those Cherenkov photons which are least delayed by scattering in the ice. The reconstructed track direction is defined by the velocity vector \vec{V} .

Because of the simple straight line hypothesis, and because the linefit does not take into account photon propagation through the ice, the reconstruction accuracy improves if only hits close to the particle track are included in the fit. This is achieved by selecting hits in which a large number of photons are detected. A zenith angle resolution ($\sim 2^\circ$), defined here as the median difference between the true and reconstructed zenith direction for simulated events at the penultimate cut level, is achieved by only using hits that saturate the PMT ADC. Shown in Fig. 3 are the distances from the primary track to a saturated hit. Saturated hits are up to ~ 10 m away for muons and up to ~ 60 m for the fastest monopoles. The relative closeness of the saturated hits mean timing information will be less affected by scattering and absorption, improving the accuracy of reconstructing the particle.

In addition, all hits in which the saturation occurred more than 500 ns after the DOM launched are excluded from the fit. These are saturated hits where the launch time is caused by something other than the saturating particle, e.g. dark noise. This creates errors in the reconstruction since the hit information includes a time well before the physics event. Roughly 0.05% of the saturate hits are removed by this criterion.

The robustness of the linefit against timing inaccuracies in the hardware was studied by smearing the hit times consistent with the frequency of the internal DOM clock. This resulted in a negligible change on the reconstruction accuracy ($< 1\%$) and final sensitivity ($< 1\%$).

B. Low level filter

The low level filter selects events with high Cherenkov light yield by requiring at least two of the hits to saturate (NSAT > 1). This cut reduces background by $\sim 99.5\%$ and signal by $\sim 10 - 15\%$ and ensures that the minimum required two hits are available to reconstruct the track direction.

TABLE I: Event rates in events/year for each dataset at all levels of the analysis. Includes simulated signal, background and the experimental data. For signal rates, a flux of $5 \times 10^{-17} \text{cm}^{-2} \text{sr}^{-1} \text{s}^{-1}$ is assumed.

Dataset	Online Filter	Low Level	Quality Cuts	Final
Experimental Data	3.15×10^7	6.55×10^5	1.21×10^5	0
Corsika Proton	7.35×10^6	2.65×10^3	2.93×10^4	3.61×10^{-4}
Corsika Iron	5.14×10^6	2.20×10^3	6.19×10^4	4.70×10^{-2}
Atm Conv ν_μ	37.9	26.4	13.6	3.45×10^{-2}
Atm Prompt ν_μ	4.9	2.83	0.334	4.12×10^{-2}
Atm Conv ν_e	1.4	0.967	8.08×10^{-6}	5.52×10^{-6}
Atm Prompt ν_e	2.0	1.86	1.43×10^{-3}	7.39×10^{-4}
Bkgrd Total	1.25×10^7	4.85×10^5	9.12×10^4	0.124
$\beta = 0.995$	100	89.2	63.4	35.6
$\beta = 0.9$	95.3	84.5	60.8	33.4
$\beta = 0.8$	81.0	70.1	46.5	22.1

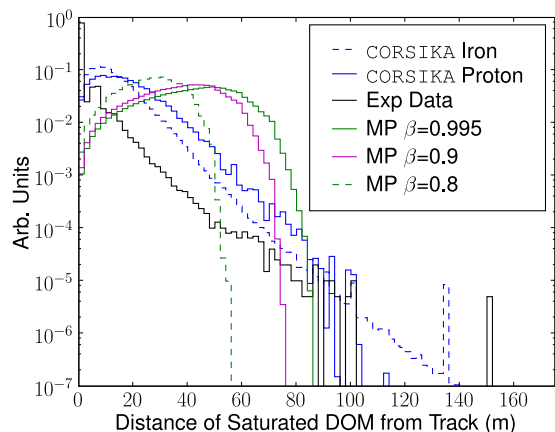


FIG. 3: Distance from particle track to saturated DOM. All histograms are normalized to 1. For CORSIKA, a track is defined by the primary cosmic ray. For data, it is defined by the reconstructed track. Events with only two saturated hits will reconstruct through the hits and produce the large spike at zero.

C. Quality Cuts

Background events which record several saturated hits as a result of a bright secondary cascade result in all the hits occurring within a small time interval and being located in a relatively small volume. This results in poor reconstructions because of the small lever arm to determine the overall directionality of the hits. These are removed by requiring the saturated hits to occur over at least 750 ns. This reduces background by $\sim 80\%$. The signal is reduced by $\sim 30\%$, but these generally represent poor quality events that only saturate one or two strings.

A second category of mis-reconstructed events are caused when multiple muon bundles travel through the detector in a single trigger window. These events are problematic for this analysis when one saturates a DOM in the bottom of the detector before a second saturates a

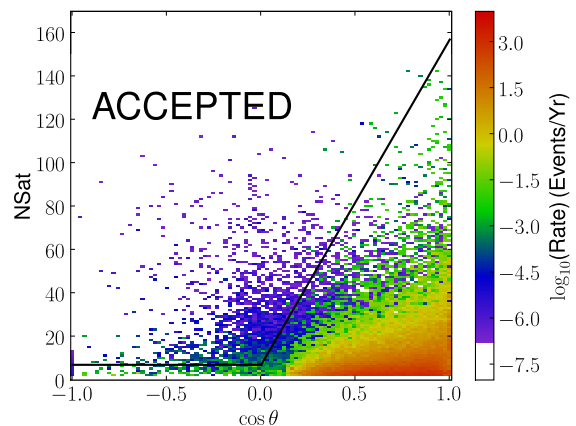


FIG. 4: Final cut on simulated background. This includes atmospheric muon bundles and atmospheric neutrinos. Data are histogrammed with bin sizes of $\text{NSat}=1$ and $\cos\theta=0.022$.

DOM near the top, resulting in an up-going reconstruction. The large majority are separated enough in time so that the speed of the reconstruction (Eq. 2) connecting the two events is very low. These are eliminated by removing events with a reconstructed speed below 0.2 m/ns. A second cut requiring the difference in $\cos\theta$ between the reconstruction on all hits versus saturated hits to be within 0.6 of 0.0 eliminates these events that happen close in time. The combined effect of these cuts is to remove $\sim 1\%$ of the background and signal.

D. Final Cut

The optimized final selection is a piece-wise, linear cut on NSAT and $\cos\theta$. Figures 4 and 5 show the distribution of simulated background and the fastest monopole signal in this plane, along with the cut. The background is dominated by atmospheric muon bundles, which have

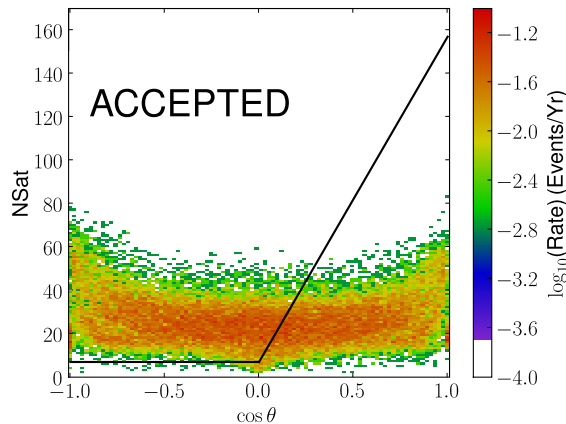


FIG. 5: Final cut on $\beta = 0.995$ signal monopoles. Data are histogrammed with bin sizes of $\text{NSat}=1$ and $\cos\theta=0.022$.

a rate ~ 5 orders of magnitude larger than the atmospheric neutrinos. They are essentially all down-going, with the more vertical events producing more saturated hits. Hence, the final cut is chosen to be on NSAT with an angular dependence: constant in the up-going region ($\cos\theta < 0.0$) and linearly increasing in strength in the down-going region ($\cos\theta > 0.0$). These two cuts join at $\cos\theta = 0.0$. The two numbers that describe this cut are the value of the NSAT cut for the up-going region ('base') and the linear steepness for the down-going region ('slope'). The final cut is given by:

$$\text{NSAT} > \begin{cases} \text{base} & \text{if } \cos\theta \leq 0 \\ \text{base} + \text{slope} * \cos\theta & \text{if } \cos\theta > 0 \end{cases} \quad (3)$$

A scan was made through possible values of the base from 0 to 25 in increments of one and the slope from 0 to 250 in increments of five. For each possible value, the MRF [24] is found using the event expectation from simulation. Figure 6 displays the result of the scan, showing the stability of the minimization. The highlighted value corresponds to the minimum with a base of 7 and a slope of 150. The final cut resulted in a background expectation of 0.124 events/year and signal efficiencies ranging between $\sim 47\%$ to 56% relative to the penultimate cut.

V. UNCERTAINTIES

Uncertainties were studied largely with Monte Carlo simulations. Table II contains the results. The large relative background uncertainty is acceptable given the small absolute event rate. Uncertainties consisted of three types: (1) Theoretical uncertainties in the simulated models, (2) Uncertainties in the detector response, and (3) Statistical uncertainties.

Theoretical uncertainties include the shape and normalization of the background energy spectrum for both

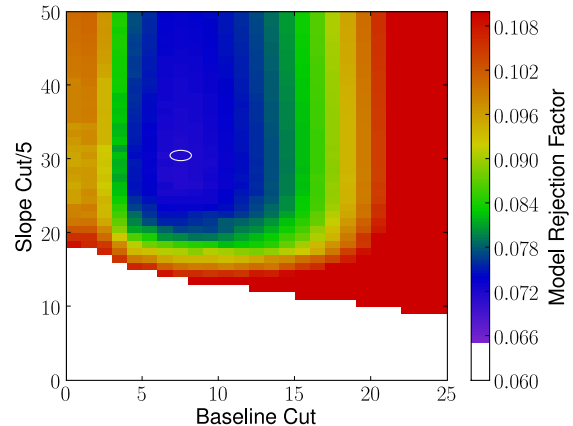


FIG. 6: Scan of Model Rejection Factors for final cut optimization. The circle corresponds to the minimum value.

the atmospheric muons and neutrinos. In addition, the cross section uncertainty modeled in both MMC and ANIS is studied. Detector uncertainties include uncertainties in the scattering and absorption parameters of the ice and the efficiency of the DOM.

For atmospheric muon background, the dominant uncertainty is from the cosmic ray energy spectrum. For both elements, the parameters of the assumed broken power-law (break energy, power-law indices below and above the break, and absolute normalization) were varied within the uncertainties in the 2-component model [18]. For iron, the extreme case of no break is taken as the upper end of the uncertainty since the expected break occurs beyond the fit region of the model. Since the final CORSIKA sample is overwhelmingly high energy iron primaries above 10^{10} GeV, it is very sensitive to changes in the spectral weighting values.

The conservative nature of this assumption is to allow for uncertainties at the high energy range that are not easily tested by simulation. Despite this extreme, the absolute uncertainty is still less than 0.5 events/year. Signal is more robust due to the brighter light yield. This allows a larger sample to pass the final cuts relative to background causing it to be less sensitive to variations in the detector response.

VI. RESULTS

The optimized cut is then applied to the full experimental data sample. No events survived on an expected background of 0.124 events, resulting in a Feldman and Cousins upper limit of 2.44 at the 90% C.L. [26]. The final distribution is shown in Fig. 7.

The final flux limit is calculated incorporating the systematic and statistical uncertainties using the profile log-likelihood method implemented in the POLE++ program [27].

TABLE II: Relative uncertainties for predicted event rates of background and signal. Total uncertainties found by adding absolute rate deviations in quadrature.

Uncertainty	Background				Signal		
	CORSIKA	ν_μ	ν_e	Total	$\beta = 0.8$	$\beta = 0.9$	$\beta = 0.995$
Normalization	26%	11%	< 1%	12%	-	-	-
Spectrum	990%	22%	39%	380%	-	-	-
MMC cross-section	10%	10%	-	7.4%	-	-	-
ν cross-section	-	6.4%	6.4%	4.0%	-	-	-
DOM Efficiency	27%	38%	38%	25%	5.8%	4.8%	1.4%
Ice Properties	78%	40%	71%	40%	7.1%	4.2%	0.2%
Statistical	22%	14%	19%	12%	0.9%	0.7%	0.7%
TOTAL	990%	64%	110%	382%	9.2%	6.5%	1.7%

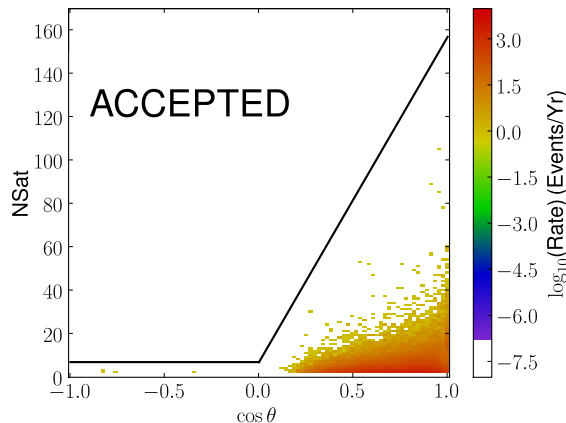


FIG. 7: Final cut on the full experimental data sample. Data is histogrammed with bin sizes of NSat=1 and $\cos\theta=0.022$.

TABLE III: Final sensitivities and limits (90% C.L.) on the flux of magnetic monopoles at detector in $\text{cm}^{-2}\text{sr}^{-1}\text{s}^{-1}$

	$\beta = 0.8$	$\beta = 0.9$	$\beta = 0.995$
Sensitivity	6.10×10^{-18}	3.94×10^{-18}	3.73×10^{-18}
Final Limit	5.57×10^{-18}	3.56×10^{-18}	3.38×10^{-18}

Table III displays the resulting sensitivities and final limits on the flux of magnetic monopoles at the detector at the 90% C.L. Figure 8 shows this result compared with previous searches from neutrino telescopes.

VII. DISCUSSION

In order to describe the results as pertaining to an isotropic flux at the surface of the Earth, the efficiency of the analysis as a function of zenith is combined with the acceptance of relativistic magnetic monopoles through the Earth. The previous AMANDA analysis did a similar procedure [6].

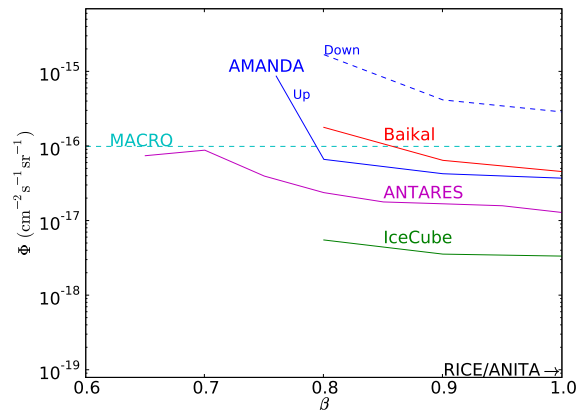


FIG. 8: Flux limits (90% C.L.) at the detector as a function of β . Includes results from AMANDA [6], Baikal [28], ANTARES [5], MACRO [7], RICE [8], and ANITA [9]

A. Angular Acceptance Through the Earth

For an isotropic, mono-energetic flux $\Phi_{\gamma_s, M}$ of magnetic monopoles with mass M and kinetic energy $E_{\text{Kin}} = M(\gamma_s - 1)$ at the Earth's surface, the resulting γ of the monopole flux at the detector is calculated for $\cos\theta$ values in increments of 0.1. The energy loss is modeled using Ahlen's stopping power formula for collisional loss [23] and code from ANITA [9] for pair production and photo-nuclear losses.

Figure 9 shows the angular acceptance of relativistic magnetic monopoles traveling through the Earth. Each line indicates the boundary between the mass and kinetic energy values which allow the monopole to reach IceCube at a particular speed threshold for a given zenith. For instance, if the mass and kinetic energy are in the region above the $\cos\theta = -1.0$ line, these describe a magnetic monopole that can remain relativistic traveling the diameter of the Earth, while those above the $\cos\theta = 1.0$ can remain relativistic traveling through the atmosphere and the ~ 2 km of South Polar ice to reach the detector.

The shape of the lines can be understood by consider-

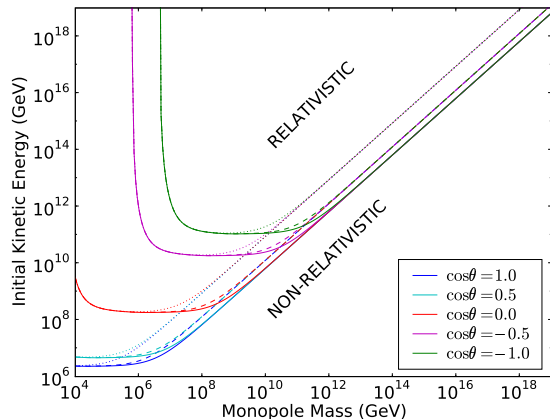


FIG. 9: Parameter space of magnetic monopoles at the Earth's surface required to reach the IceCube detector at relativistic speeds. Dotted is for a speed threshold of $\beta = 0.995$, dashed for $\beta = 0.9$, and solid for $\beta = 0.8$.

ing the full acceptance ($\cos\theta = -1.0$) case:

- * The collisional energy loss straight up through the Earth is $\sim 10^{11}$ GeV. This loss is not enough to slow relativistic magnetic monopoles with masses above $\sim 10^{12}$ GeV to sub-relativistic speeds. Therefore, the acceptance is determined solely by the starting energy.
- * Magnetic monopoles with masses between $\sim 10^7 - 10^{12}$ GeV can still reach the detector so long as there is enough kinetic energy to overcome the collisional loss. Hence, the line flattens out around $\sim 10^{11}$ GeV.
- * For magnetic monopoles with masses below $\sim 10^7$ GeV, the necessary starting energy begins to increase to overcome the increasing effect of pair production and photo-nuclear energy losses, which begin to dominate for $\gamma \sim 10^4$.

B. Angular Acceptance of Analysis

The analysis is much more sensitive to an up-going signal, due to the large atmospheric muon bundle background. This is described quantitatively by calculating the effective area as a function of zenith. The effective area corresponds to the cross sectional area of an ideal detector with 100% efficiency. Using the same $\cos\theta$ bins as above, the effective area is given by:

$$A_{\text{eff}}^{\gamma}(\cos\theta) = A_{\text{gen}}^{\gamma} \frac{N_{\text{det}}^{\gamma}(\cos\theta)}{N_{\text{gen}}^{\gamma}(\cos\theta)} \quad (4)$$

where A_{gen}^{γ} is the area of the generation plane for a given γ and $N_{\text{det}}^{\gamma}/N_{\text{gen}}^{\gamma}$ is the fraction of magnetic monopoles generated that survive the final analysis cut.

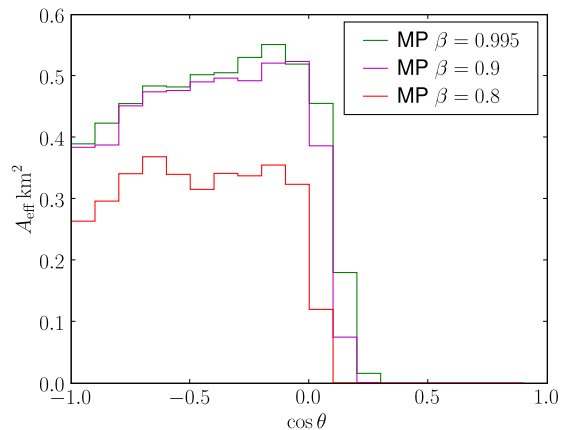


FIG. 10: Effective Area for each $\cos\theta$ bin.

Figure 10 shows the result of the three generated speeds. From Section III B, $A_{\text{gen}}^{\gamma} = 1.33 \text{ km}^2$ and $N_{\text{gen}}^{\gamma}(\cos\theta) = N_{\text{gen}}^{\gamma}/20 = 5000$, since the generated flux is isotropic. This is conservatively generalized to any speed at the detector by treating the effective area as a step function, e.g. $A_{\text{eff}}^{\gamma > 10} = A_{\text{eff}}^{\gamma = 10}$, etc. For $\beta < 0.8$, the effective area is set to zero.

C. Limits on Isotropic Fluxes at the Earth's Surface

The final limit on a flux with given mass and kinetic energy at the Earth's surface ($\Phi_{90\% \text{C.L.}}^{\gamma_s, M}$) is calculated by scaling a reference flux with the ratio of the Feldman-Cousins upper limit ($\mu_{90\%}$) [26] to the expected number of signal events seen in the detector using the reference flux. The expected signal event number is found by going through each $\cos\theta$ bin and determining (1) what speed the monopole will have at the detector (γ_d) based on Section VII A and (2) calculating the effective area for that speed and $\cos\theta$ bin based on Section VII B. The final flux limit becomes:

$$\Phi_{90\% \text{C.L.}}^{\gamma_s, M} = \frac{\mu_{90\%}(N_{\text{obs}} = 0.0, N_{\text{bkg}} = 0.124)}{N_{\text{sig}}(\Phi_{\text{Ref}}^{\gamma_s, M})} \Phi_{\text{Ref}}^{\gamma_s, M} \quad (5)$$

$$N_{\text{sig}} \approx T_{\text{live}} \Phi_{\text{Ref}}^{\gamma_s, M} 2\pi \sum_{i=1}^{20} (\Delta \cos\theta)_i A_{\text{eff}}^{\gamma_d}(\cos\theta_i) \quad (6)$$

$T_{\text{live}} = 2.06 \times 10^7 \text{ s}$ is the total livetime of the analyzed data set, $N_{\text{bkg}} = 0.124$ is the final background expectation from Table I, $\Delta \cos\theta = 0.1$ is the width of the $\cos\theta$ bins, and the 2π arises from the azimuthal symmetry of the Earth. For most tested values of γ_s, M , the final speed is the same for all bins and the flux limit calculation returns the same answer as Table III.

To place this result in context, Fig. 11 displays the current best experimental flux limits over a wide range of mass and kinetic energy values of magnetic monopoles.

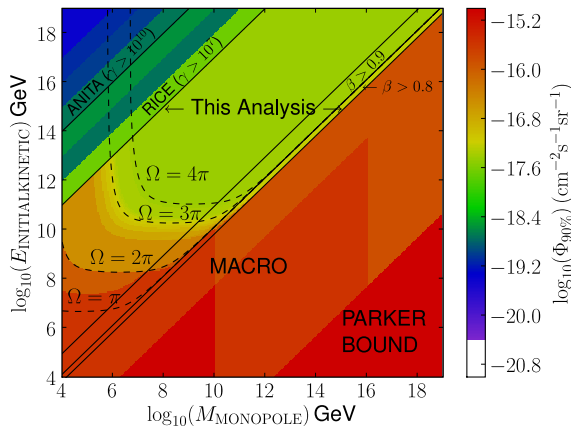


FIG. 11: Final flux limits (90% C.L.) as function of monopole mass and kinetic energy at Earth’s surface. For relativistic mass and energies, only the most restrictive limit is displayed. Includes the Parker Bound [10] and results from MACRO [7], RICE [8], and ANITA [9]. For numerical values of the final result for this analysis, see [29].

Below $\gamma = 1.67$ the analysis does not apply as the monopoles fall below the Cherenkov threshold, while above $\gamma = 10^7$, the radio neutrino detectors offer better sensitivity.

For the range of mass/kinetic energy pairs resulting in $1.67 < \gamma < 10^7$, this analysis provides in general the best flux limits to date. The exception occurs for the smallest masses and kinetic energies, where attenuation in the Earth affects the signal acceptance. To help guide the eye, lines showing the angular acceptance solid angle Ω for the $\beta = 0.9$ magnetic monopoles are included. The solid angle is found by multiplying 2π by the range of $\cos\theta$ for which the mass and energy combination can reach the detector. Hence the shape matches Fig. 9. As the solid angle approaches 2π , acceptance below the horizon is lost and the limit becomes much weaker.

For the cases where $\gamma > 10^4$, the flux limit from this analysis is conservative, as the monopole would have a large light contribution from secondary cascades which are not yet included in the simulation. These will make the event brighter in the detector and increase the selection efficiency.

VIII. CONCLUSION

This analysis is the first search for magnetic monopoles using the next generation of neutrino telescopes. A final flux limit of $\Phi_{90\% \text{C.L.}} = 3.38 \times 10^{-18} \text{cm}^{-2} \text{sr}^{-1} \text{s}^{-1}$ for $\beta \geq 0.995$ is found. For speeds down to $\beta = 0.8$, the flux limit is slightly higher. This applies to an isotropic flux at the Earth’s surface for relativistic magnetic monopoles with mass above $\sim 10^6 \text{GeV}$ and energy above $\sim 10^{10} \text{GeV}$ (Fig. 11). Even with a single year of data operating at

$\sim 20\%$ of the final instrumented volume, experimental flux limits are achieved that are a factor of 4 below the current best constraints up to $\gamma \sim 10^7$ and provide a good compliment to the more sensitive radio searches for ultra-relativistic monopoles.

This analysis does not follow IceCube’s usual procedure of a blind analysis. An original analysis performed on the data was done in a blind fashion, with cuts being determined by simulation datasets along with a 10% ‘burn’ sample of experimental data. It aimed to enhance the sensitivity to slower monopoles by binning the data based on speed reconstruction. Unblinding revealed deficiencies in the background simulation to reproduce the tails of the speed distribution where the slower signal should be and allowed obvious background events into the final sample. After determining no monopole events were recorded, the analysis reported here is performed with cuts optimized on improved simulation and not the experimental data. The only changes involve a slight tightening of quality cuts motivated by the new simulation and abandoning the binning based on speed reconstruction. For a full description of the original analysis, final event rejection, and motivation for changes, see [29].

Preliminary work on the 2008 data run shows that the increased detector size and improvements to the analysis method provide a further factor of 4 reduction in the sensitivity [30]. With more data and refined techniques, IceCube and other neutrino telescopes will continue to prove valuable in searches for magnetic monopoles in the relativistic regime.

Acknowledgments

We acknowledge the support from the following agencies: U.S. National Science Foundation-Office of Polar Programs, U.S. National Science Foundation-Physics Division, University of Wisconsin Alumni Research Foundation, the Grid Laboratory Of Wisconsin (GLOW) grid infrastructure at the University of Wisconsin - Madison, the Open Science Grid (OSG) grid infrastructure; U.S. Department of Energy, and National Energy Research Scientific Computing Center, the Louisiana Optical Network Initiative (LONI) grid computing resources; National Science and Engineering Research Council of Canada; Swedish Research Council, Swedish Polar Research Secretariat, Swedish National Infrastructure for Computing (SNIC), and Knut and Alice Wallenberg Foundation, Sweden; German Ministry for Education and Research (BMBF), Deutsche Forschungsgemeinschaft (DFG), Research Department of Plasmas with Complex Interactions (Bochum), Germany; Fund for Scientific Research (FNRS-FWO), FWO Odysseus programme, Flanders Institute to encourage scientific and technological research in industry (IWT), Belgian Federal Science Policy Office (Belspo); University of Oxford, United Kingdom; Marsden Fund, New Zealand; Australian Research Council; Japan Society for Promo-

tion of Science (JSPS); the Swiss National Science Foundation (SNSF), Switzerland.

-
- [1] P.A.M. Dirac, Proc. R. Soc. A **133** 60 (1931).
 [2] G. t'Hooft, Nucl. Phys. B **79** 276 (1974);
 A. Polyakov, Pis'ma Zh. Eksp. Teor. Fiz. **20** 430 (1974).
 [3] S. D. Wick, T.W. Kephart, T.J. Weiler, and P.L. Biermann, Astropart. Phys. **18** 663 (2003).
 [4] D. Tompkins, Phys. Rev. **138** B248 (1965).
 [5] S. Adrián-Martínez et al. (ANTARES Collaboration), Astropart. Phys. **35** 634 (2012). arXiv:1110.2656v1
 [6] R. Abbasi et al. (IceCube Collaboration), Eur. Phys. J. C **69** 361 (2010).
 [7] M. Ambrosio et al. (MACRO Collaboration), Eur. Phys. J. C **25** 511 (2002). [arXiv:hep-ex/0207020v2]
 [8] D.P. Hogan, D.Z. Besson, J.P. Ralston, I. Kravchenko, and D. Seckel, Phys. Rev. D **78** 075031 (2008). arXiv:0806.2129v2 [astro-ph]
 [9] M. Detrixhe et al. (ANITA Collaboration), Phys. Rev. D **83** 023513 (2011). arXiv:1008.1282v2 [astro-ph.HE]
 [10] E.N. Parker, Astrophys. J. **160** 383 (1970).
 [11] M. S. Turner, E.N. Parker, and T.J. Bogdan, Phys. Rev. D. **26** 1296 (1982).
 [12] F.C. Adams et al., Phys. Rev. Lett. **70** 2511 (1993).
 [13] A. Karle (IceCube Collaboration), in Proc. 31st ICRC, Lodz, Poland (2009). arXiv:1003.5715; see also, <http://icecube.wisc.edu>
 [14] R. Abbasi et al. (IceCube Collaboration), Nucl. Instrum. and Methods A **601** 294 (2009).
 [15] R. Abbasi et al. (IceCube Collaboration), Nucl. Instrum. and Methods A **618** 139 (2010).
 [16] R. Abbasi et al. (IceCube Collaboration), Phys. Rev. D. **82** 072003 (2010).
 [17] D. Heck et al., Technical Report 6019, Forschungszentrum Karlsruhe (1998).
 [18] R. Glasstetter et al., Proc. 26th ICRC, Salt Lake City, USA (1999). HE.2.2.03
 [19] D. Chirkin and W. Rhode, arXiv:hep-ph/0407075v2
 [20] A. Gazlzov and M. Kowalski, Comput. Phys. Commun. **172** 203 (2005).
 [21] M. Honda, T. Kajita, K. Kasahara, S. Midorikawa, and T. Sanuki, Phys. Rev. D **75** 043006 (2007). arXiv:astro-ph/0611418v3
 [22] R. Enberg, M.H. Reno, and I. Sarcevic, Phys. Rev. D **78** 043005 (2008).
 [23] S.P. Ahlen, Phys. Rev. D **17** 229 (1978).
 [24] G. Hill and K. Rawlins, Astropart. Phys. **19** 393 (2003). arXiv:astro-ph/0209350v1
 [25] J. Ahrens et al. (AMANDA Collaboration), Nucl. Instrum. Methods A **524** 169 (2004).
 [26] G. J. Feldman and R. D. Cousins, Phys. Rev. D **57** 3873 (1998).
 [27] F. Tegenfeldt and J. Conrad, Nucl. Instrum. Meth. A **539** 407 (2005). arXiv:physics/0408039v2
 [28] V. Aynutdinov et al. (BAIKAL Collaboration), Astropart. Phys. **29** 366 (2008).
 [29] B. Christy, Ph.D. thesis, University of Maryland College Park (2011). <http://hdl.handle.net/1903/12293>
 [30] J. Posselt and B. Christy for the IceCube Collaboration, Proc. 32nd ICRC, Beijing, China (2011). arXiv:1111.2738v1 [astro-ph.HE]